

Metastable high entropy alloys: An excellent defect tolerant material for additive manufacturing



Priyanshi Agrawal^{a,b,1}, Ravi Sankar Haridas^{a,b,1}, Saket Thapliyal^{a,b}, Surekha Yadav^{a,b}, Rajiv S. Mishra^{a,b,*}, Brandon A. McWilliams^c, Kyu C. Cho^c

^a Department of Materials Science and Engineering, University of North Texas, Denton, TX, 76203, USA

^b Advanced Materials and Manufacturing Processes Institute, University of North Texas, Denton, TX, 76203, USA

^c Weapons and Materials Research Directorate, CCDC Army Research Laboratory, Aberdeen Proving Grounds, Aberdeen, MD, 21005, USA

ARTICLE INFO

Keywords:

Fatigue
High entropy alloys
Transformation induced plasticity
Additive manufacturing
Probabilistic fatigue life prediction

ABSTRACT

Fatigue failure is ubiquitous in structural components. In additively manufactured (AM) components, the processing induced defects limit the fatigue performance. Further, the stochastic nature of defects in laser-powder bed fusion (L-PBF) make it difficult to predict the fatigue life in these components. In this work, we explored exceptional work hardening (WH) of a metastable Fe₄₀Mn₂₀Co₂₀Cr₁₅Si₅ high entropy alloy (CS-HEA) to obtain high fatigue-resistance with L-PBF. Further, a fatigue life estimation tool based on the statistical size distribution of microstructural entities such as grains, pores and solid-state inclusions and, their mutual interaction was used to estimate the fatigue life of as-printed material. Upon deformation, CS-HEA exhibited γ (f.c.c.) \rightarrow ϵ (h.c.p.) martensitic transformation and subsequent twinning in ϵ (h.c.p.) phase. Such deformation behavior resulted in sustained WH and is specifically beneficial in the vicinity of critical pores. A high normalized fatigue strength of 0.65 with respect to the yield strength was thus obtained in as-printed condition. Further, the model accurately predicted extended crack initiation life for CS-HEA. The current work therefore provides guidance towards developing defect-tolerant alloys for L-PBF and presents a tool for estimation of fatigue life of AM alloys with unconventional WH behavior.

1. Introduction

Additive manufacturing is a novel process that has revolutionized the manufacturing industries. Well-known advantages of additive manufacturing include fewer geometrical constraints, which benefit industries by inspiring development of new design paradigms to manufacture lighter and more complex parts at lower cost, with shorter lead time and no wastage [1]. Additionally, additive manufacturing has facilitated the manufacture of functionally-graded parts as well as remote manufacturing and repair on demand [2,3]. The aforementioned benefits of additive manufacturing incentivized industries such as aerospace, marine, biomedical and military, to fabricate components for structural as well as functional applications. However, a comprehensive understanding of structure-property correlation in additively manufactured (AM) alloys is critical, especially for parts that will be subjected to dynamic loading.

AM materials are known to be associated with processing-induced

defects such as pores, micro cracks and inclusions that adversely affect the mechanical properties of AM materials [4,5]. Although defect volume fraction can be reduced by optimizing additive manufacturing process parameters, complete elimination is still infeasible [6,7]. Hence, design and development of advanced materials and alloys are required to take complete advantage of the process in spite of mentioned shortcomings. High entropy alloys (HEAs) are a special class of materials in which the primary deformation mechanisms can be tuned by adjusting their chemical composition [8,9]. The microstructure and properties of such alloys can be tailored to achieve higher defect tolerance. For example, in transformation induced plasticity (TRIP) HEAs, the stress concentration (SC) near the defects has the potential to transform the material around the defects which delays crack initiation and retards crack propagation, thereby providing a recourse to design defect-tolerant materials for structural applications [10,11]. Non-equiautomic HEAs, also called complex concentrated alloys or compositionally complex alloys (CCAs), provide wide compositional

* Corresponding author. Department of Materials Science and Engineering, University of North Texas, Denton, TX, 76203, USA.

E-mail address: Rajiv.Mishra@unt.edu (R.S. Mishra).

¹ Contributed equally for first authorship.

space to exploit the benefits of previously established deformation mechanisms such as TRIP and twinning-induced plasticity (TWIP). Li et al. [12] used the metastability of phases synergized with high entropy to activate multiple deformation mechanisms that exhibited adequate strength and ductility synergy. In our earlier study [13], we introduced AM CS-HEA, which showed an excellent combination of strength and ductility due to the TRIP effect, where face centered cubic (f.c.c.) phase γ transforms to hexagonal close packed (h.c.p.) phase ϵ -martensite and partitioning of plastic strain among γ and ϵ phases assisted by non-basal slip and twinning in newly-formed ϵ phase.

The main challenge in adopting AM components for structural applications is their poor fatigue resistance. Damage accumulation during fatigue loading results in catastrophic failure of structural materials. Defects such as pores and microcracks in AM materials deteriorate fatigue performance in that the defects act as fatigue crack initiation sites [14]. Also, surface roughness of AM components greatly affects fatigue life. Effect of surface roughness on fatigue life of AM component was studied and a critical valley depth/valley spacing ratio below which fatigue life is unaffected by surface roughness was reported [15]. However, for the present study, since samples are polished, the effect of surface roughness on fatigue is not considered. Thus far, studies on fatigue performance of AM materials are limited to only a few alloy systems; namely Ti-6Al-4V, Ni-based superalloys, aluminum alloys and steels [14,16–19]. Therefore, development of novel alloys for AM and understanding the underlying deformation mechanisms key to the fatigue behavior of these alloys are necessary.

Activation of additional deformation mechanisms along with conventional dislocation hardening provide sustained work hardening (WH) to the materials and in turn promote the desired response to fatigue cracks. In the present study we introduce a fatigue-resistant alloy using laser powder bed fusion (LPBF), a non-equiautomic TRIP-enabled Fe₄₀Mn₂₀Co₂₀Cr₁₅Si₅ HEA (henceforth denoted as CS-HEA). In CS-HEA, TRIP and TWIP deformation mechanisms have been activated by composition-based tuning of the stacking fault energy. Metastability of γ f.c.c. phase (parent phase) is increased by reducing the free energy difference between γ and ϵ phases ($\Delta G^{\gamma \rightarrow \epsilon}$). Moreover, the reduction in the $\Delta G^{\gamma \rightarrow \epsilon}$ is directly related to decrease in stacking fault energy of the f.c.c. phase [20]. Reduction in stacking fault energy gives rise to different deformation mechanisms; the primary deformation mode observed changes from slip (SFE > 40 mJ m⁻²) to TWIP (20 $>$ SFE < 40 mJ m⁻²) or TRIP (SFE < 15 mJ m⁻²) in f.c.c. metals and alloys [20]. In additive manufacturing, process-induced defects are unavoidable; and sites such as pores and microcracks are potential crack initiation sites as they result in stress concentration. However, materials that exhibit additional deformation mechanisms such as TRIP or TWIP, stress concentration in the vicinity of the pores or cracks results in activation of transformation or twining [21]. Transformation and twining provide sustained WH and retardation/branching of cracks [22,23]. This study focused on developing an alloy for LPBF that exhibits high fatigue crack growth resistance despite the presence of pores. Furthermore, we examined the implications of the TRIP effect triggered by $\gamma \rightarrow \epsilon$ transformation and twining in ϵ phase on the fatigue properties of as-printed material containing process-induced defects.

In order to optimize process parameters and produce parts with minimum defects, CS-HEA was printed using LPBF with different processing parameters. Microstructural analysis was performed to correlate the properties and to optimize the printing parameters. Fatigue tests were performed on samples milled out from printed blocks with optimized parameters. For such a new alloy system, understanding the complex fatigue behavior and its correlation with statistical distribution of defects and grain size distribution is difficult. Several models to predict fatigue life using probabilistic modeling for conventionally processed alloys have been already developed [24–28]. Haridas et al. [17] extended probabilistic fatigue modeling to AM Al alloys by considering the statistical distribution of pores, unfused powder particles and grains. Given the ubiquity of pores in AM, an interaction of pores, inclusions

and grain boundaries is more likely to occur. This tool is therefore useful for predicting fatigue life of AM alloys. This probabilistic fatigue model has been applied to CS-HEA to understand the fatigue behavior by correlating fatigue performance with different fatigue crack initiation and crack propagation indicators.

2. Experimental details

The AM specimens were manufactured using Aconity MIDI (Aconity 3D GmbH) equipped with a single (maximum 1000 W) fiber laser. Pre-alloyed, gas-atomized Fe₄₀Mn₂₀Co₂₀Cr₁₅Si₅ (at. %) powder (chemical composition as provided in Table 1), with powder particle size in the range of 15–45 μ m, was used for printing. AM parameters were optimized for minimal defects such as porosity. Layer thickness (t), scanning speed (v) and rotation between adjacent layers (ϕ) were kept constant at 0.04 mm, 800 mm/s and 67°, respectively. In recent days, $\phi = 67^\circ$ is used as the standard value to print AM alloys with equiaxed microstructure and isotropic properties [16]. Laser power (P) and hatch spacing (h) were varied to adjust the energy density (E). The value of parameters used for printing are provided in Table 2. E (J/mm³) for the combination of printing parameters can be calculated using Eqn. (1).

$$E = \frac{P}{vht} \quad (1)$$

The printed CS-HEA block was 30 mm long, 15 mm wide and 4 mm thick. Printing was carried out in the protective atmosphere of Ar, keeping the O₂ content below 0.01% throughout the LPBF process.

The as-printed CS-HEA specimens for microstructural analysis were machined using an EDM. The samples were then mechanically polished to 0.02 μ m to get a mirror-like surface finish. Optical micrographs of the specimens were taken using Nikon Eclipse ME600 optical microscope at 10X. Electron backscattered diffraction (EBSD) scans were done on FEI Nova NanoSEM230 with Hikari EBSD camera attachment operating at 20 kV and 6.1 nA current and 75 nm step size using a 70° pre-tilt holder. The EBSD data was analyzed using TSL OIM 8 software. Backscattered imaging (BSE) and fractography of the specimens were performed at an operating voltage of 20 kV with a beam current of 6.1 nA and a working distance of 10 mm.

For tensile testing, dog-bone shaped specimens of thickness 1 mm, gauge length 5 mm and width 1.25 mm oriented along the build direction were machined in an EDM. For each condition, three samples were tested at room temperature at strain rate of 10⁻³ s⁻¹ to confirm reproducibility of the results. The numerical values of mechanical properties mentioned in the following sections are average of the three tests performed. Fully reversed ($R = -1$) bending fatigue tests were performed using a custom-made tabletop mini-fatigue testing machine at 20 Hz. Details of the fatigue machine have been reported elsewhere [29]. Fatigue samples were milled from the printed block in the direction parallel to the axis of build (Fig. 1 (a)). Sample dimensions and a schematic of specimen orientation with respect to build direction are presented in Fig. 1 (b). Tensile and fatigue samples were polished with SiC papers to 1200 grit, and final polishing was carried out using 0.02 μ m diamond suspension to minimize the deleterious effect of surface roughness on mechanical properties.

Table 1
Chemical composition of the pre-alloyed powder [11].

Elements	Cr	Co	Si	Mn	Fe
At. (%)	15	20	5	20	40
(Nominal)					
At. (%) (Actual)	14.8 ± 1.00	19.1 ± 1.16	5.5 ± 0.40	18.8 ± 1.08	41.8 ± 1.10

Table 2

Printing parameters used for LPBF of CS-HEA.

Sample code	Power, P (W)	Hatch spacing, h (μm)	Energy Density, E (J/mm^3)
S1	120	100	37.50
S2	120	120	31.25
S3	140	100	43.75
S4	140	120	36.45
S5	160	100	50.00
S6	160	120	41.66
S7	180	100	56.25
S8	180	120	46.87
S9	200	100	62.50
S10	200	120	52.08

3. Results

3.1. Parametric optimization

Fig. 2 (a) shows representative optical micrographs and (xi-xii) shows low magnification SEM images of the as-printed specimens the images are obtained on a plane parallel to the build direction. Although process induced pores are visible on the sample surface, absence of microcracks indicates excellent printability of CS-HEA. When the value of E is low (31.25 J/mm^3), pores are predominantly related to lack of fusion (LoF) of the powder particles. On the other hand, when E is higher than 52.08 J/mm^3 (in cases S8, S9, and S10), the more prevalent keyhole defects are observed [30]. Intermediate values of E (37.5 J/mm^3 and 43.75 J/mm^3) resulted in minimum defect density. Additionally, for specimens with same P , $h \sim 120 \mu\text{m}$ resulted in higher defect density compared to $h \sim 100 \mu\text{m}$; the possible reason for this can be inadequate overlapping of the adjacent melt-pools at higher values of h .

Relative density of as-printed CS-HEA, which is measured using Archimedes' principle, is plotted in **Fig. 2** (b) as a function of E . Theoretical density for CS-HEA is calculated as 7.816 g/cm^3 . The relative density of the as-printed CS-HEA for different parameters varies from 98.5% to 99.5%, trend in the variation of density is consistent with surface pore distribution observed in the optical micrographs. The ratio of the difference between theoretical and measured density to theoretical density was used to estimate porosity in the samples. To further confirm the porosity values image analysis was also performed on the samples. Furthermore, uniaxial tensile tests were performed on all printed CS-HEA specimens to investigate the effect of processing parameters on tensile properties. The engineering stress-strain curves of all 10 specimens are displayed in **Fig. 2** (c). The yield strength (σ_y) and the ultimate tensile strength (σ_u) of specimens varied from 460 MPa to 570 MPa and 900 MPa–1100 MPa, respectively. Although porosity is highest in S4 condition (1.7%), a substantial reduction in ductility was not observed, this may be attributed to TRIP effect as reported in Ref. [11], as well as the critical pore dimension in the gauge section of the sample. In case of S1 with $E \sim 37.50 \text{ J/mm}^3$, maximum elongation to failure (33%) was observed with combination of $\sigma_y = 550 \text{ MPa}$ and $\sigma_u = 1100 \text{ MPa}$. Due to superior combination of strength and ductility, parameters used for printing of specimen S1 were also used for printing the block for

mini-fatigue specimens.

3.2. Microstructural characterization

The representative EBSD micrographs of XZ cross section (**Fig. 3** (f)) of case S1 are displayed in the direction parallel to the build direction. Bi-modal grain morphology consisting of equiaxed and columnar grains can be observed in inverse pole figure (IPF) and image quality (IQ) maps of the specimens (**Fig. 3** (a), (b)). Grain morphology in AM alloys is controlled by G/R ratio, where G is the thermal gradient and R is the solidification rate. Higher G/R leads to columnar morphology, whereas low G/R leads to equiaxed morphology [31–33]. **Fig. 3** (c) is the phase map of as-printed CS-HEA, which shows a dual-phase microstructure with the dominance of martensitic ϵ -phase, and is similar to what we reported previously [13].

The statistical parameters of microstructural features like pores, inclusions and grain size, which are used in the fatigue life estimation model, were quantified through comprehensive SEM microscopy; details of the procedure are included in Ref. [17]. **Fig. 3** (d) and (e) show representative BSE images of an as-printed specimen, on a plane parallel to the build direction (XZ plane). The unfused powder particles near LoF pores (**Fig. 3** (d)) are considered as solid-state inclusions, as these particles can initiate fatigue cracks through interfacial cracking.

3.3. High cycle fatigue (HCF)

Fig. 4 (a) shows true and engineering stress-strain response of AM CS-HEA using optimized parameters (S1), σ_y and σ_u of the alloy of $520 \pm 30 \text{ MPa}$ and $1000 \pm 10 \text{ MPa}$, respectively. High work hardenability in CS-HEA is due to γ (f.c.c.) $\rightarrow \epsilon$ (h.c.p.) martensitic transformation (TRIP) and twinning in the transformed ϵ phase (TWIP) during deformation [8,13]. The WH exponent for as-printed CS-HEA is ~ 0.29 , whereas it is ~ 0.22 for as-cast CS-HEA, features high work hardenability in AM condition [13]. **Fig. 4** (b) presents the stress amplitude (σ_a)–number of cycles (N) curve from fully reversed ($R = -1$) bending fatigue testing. Fatigue tests were carried out following the stair-case method, where σ_a ranges from 200 to 450 MPa; i.e., σ_a/σ_y of ~ 0.4 – 0.81 , to obtain the S-N data. TRIP- and TWIP-enabled CS-HEA in as-printed condition confirms good fatigue resistance; the run-out stress amplitude (for 10^7 cycles) for the alloy is 325 MPa, which can be considered as the endurance limit (σ_f) and corresponds to $\sigma_a/\sigma_y \sim 0.65$. Very limited data is available on fatigue properties of AM HEAs. However, the AM TRIP and TWIP steels are expected to show similar response to fatigue loading, and can be used as benchmarks to compare the fatigue results in the present study. Lee et al. [34] studied the cyclic deformation behavior of selective laser melted 304 stainless steel, which shows similar deformation induced martensitic transformation or TRIP effect; the σ_f observed is $\sim 300 \text{ MPa}$ for run-out cycles of 10^7 .

The effect of LoF defects on cyclic loading performance was insignificant because of high ductility and the high hardening capacity of the material due to $\gamma \rightarrow \epsilon$ transformation. Such alloys deliver an attractive combination of excellent tensile strength and promising HCF behavior due to higher inherent damage tolerance.

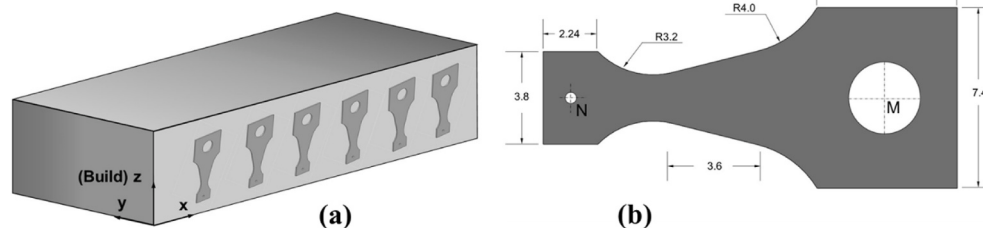


Fig. 1. (a) Schematic of fatigue sample orientation in the printed block, and (b) fatigue sample dimensions (in mm) used for mini-fatigue test.

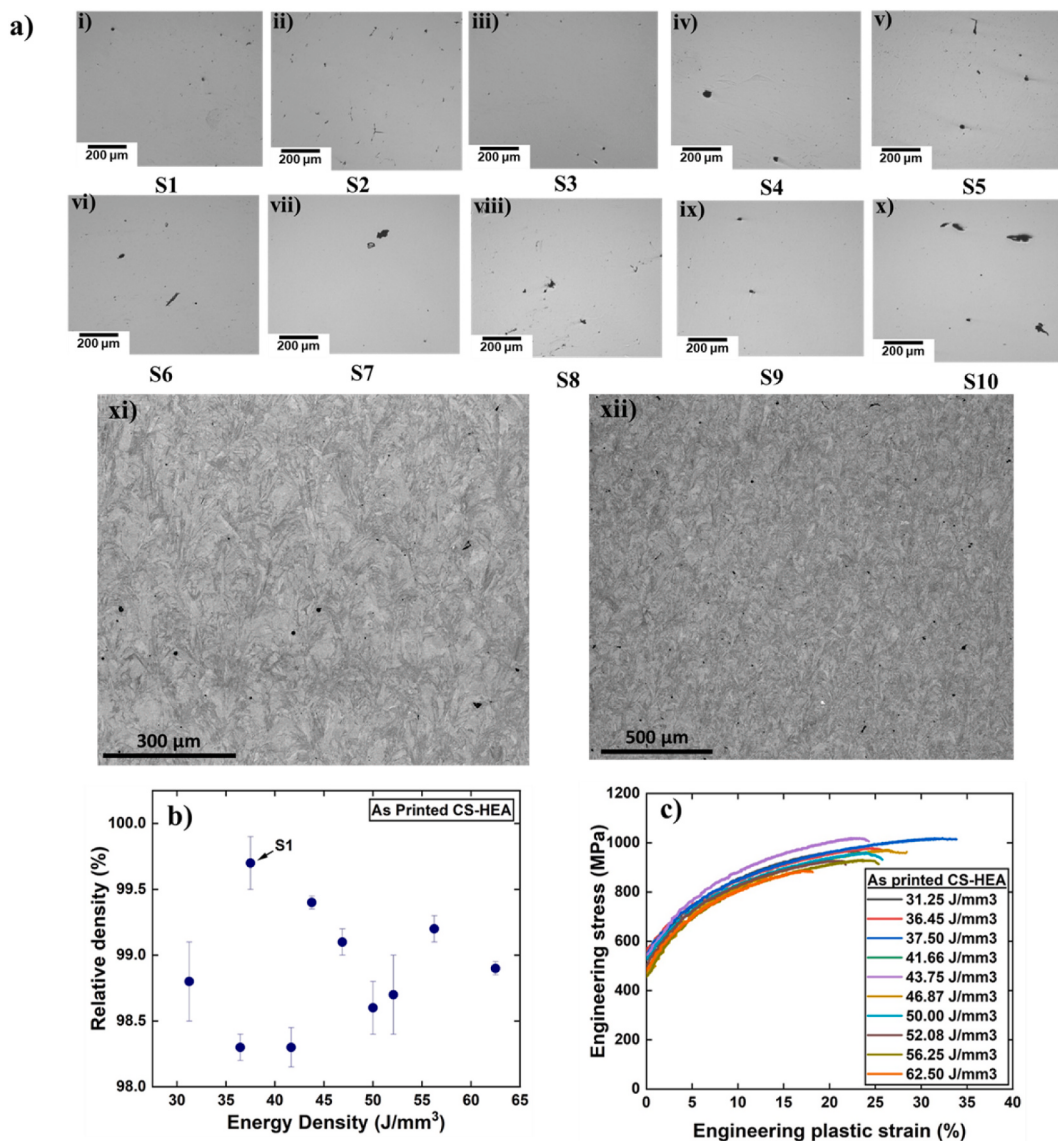


Fig. 2. (a) Optical micrograph of as-printed CS-HEA on a plane parallel to the build direction, (xi-xii) low magnification SEM images of as build CS-HEA, (b) relative density vs energy density, and (c) engineering stress-strain plot for CS-HEA printed at different parameters.

Previous research on the fatigue behavior of AM alloys has confirmed that processing defects such as pores are the potential crack initiation sites [35–38]. The fracture surfaces of the failed specimens were analyzed to identify crack initiation sites in the fatigued specimens (Fig. 5 (a, b)). Maximum flexural stress at the outer surfaces of the specimen led to the surface pores being subjected to maximum stress concentration and become expected crack initiation sites. Surface pores highlighted in the red circles (Fig. 5 (a) and (b)) are identified as the potential crack initiation sites. Indeed, crack initiated from the surface pores led to failure in the majority of the specimens; the effect of types of porosity on crack initiation will be discussed in the following section.

4. Discussion

4.1. Crack initiation and propagation during HCF

Fatigue life of metals/alloys is comprised of crack initiation life as well as subsequent crack propagation life [39]. Crack initiation life occupies the major portion of fatigue life in HCF. However, processing defects in AM materials lead to shorter crack initiation life. Hence, a damage-tolerant material design approach can be used to reduce the

deleterious effect of processing defects on fatigue life. Vast compositional space of HEAs provide opportunity to design alloys capable of activating multiple deformation mechanisms such as TRIP and TWIP which enable crack retardation. The study by Liu et al. [10] on the friction stir processed metastable HEA showed that stress concentration near the crack tip triggers $\gamma \rightarrow \epsilon$ transformation. This transformation provides localized WH to the material and retards the crack propagation rate. Being a metastable HEA, CS-HEA exhibits activation of TRIP and TWIP deformation mechanisms in AM as well as conventionally processed conditions [13,40]. In order to understand the effect of TRIP and TWIP on fatigue crack initiation and propagation in AM CS-HEA, an interrupted fatigue test was carried out. The fatigue test was halted after 8×10^4 loading cycles once the crack had initiated at a stress amplitude of 400 MPa ($\sigma_a/\sigma_y \sim 0.72$).

Fig. 6 shows the BSE images of the interrupted sample; overall crack path is displayed in Fig. 6 (a). Fig. 6 (b) confirms that the cracks initiated from various pores near the surface, and it also confirms that the instance of crack initiation from each pore is a function of stress concentration and the geometry of the pore. Haridas et al. [17] reported that an irregular pore with the same volume develops more stress concentration and is more critical than a regular pore. Fig. 6 (d) is a magnified

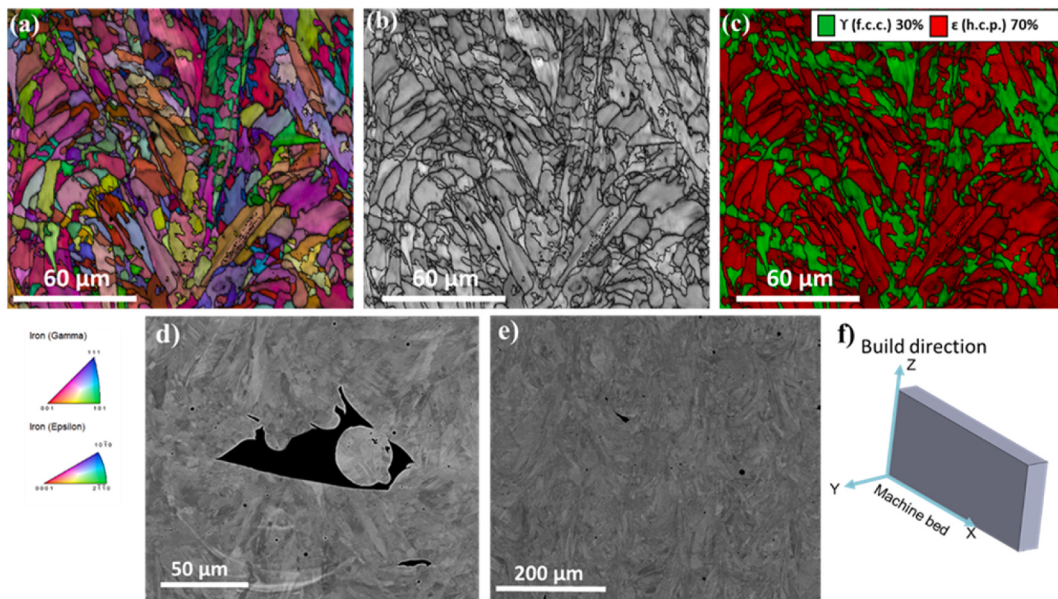


Fig. 3. SEM micrographs of as-printed specimen (a) inverse pole figure map, (b) image quality map and, (c) phase map for CS-HEA printed with optimized parameters, (d–e) back-scattered images of as-printed CS-HEA, and (f) schematic of sample orientation.

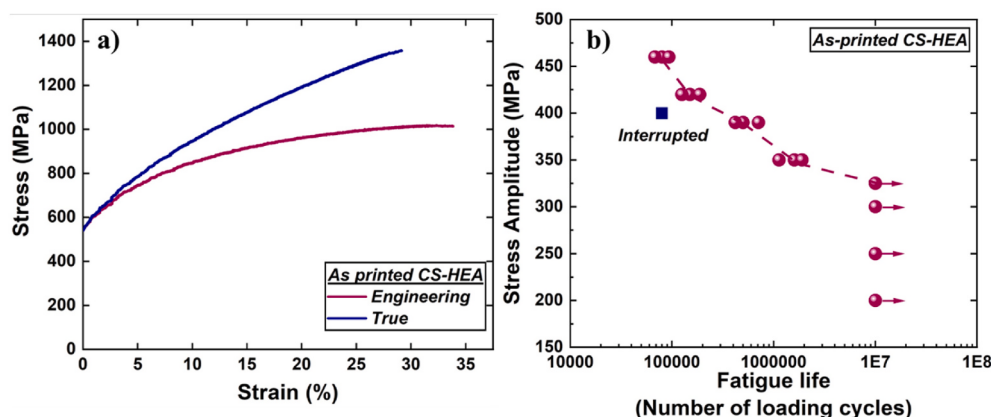


Fig. 4. (a) Tensile stress-strain response, and (b) S-N data for as-printed CS-HEA.

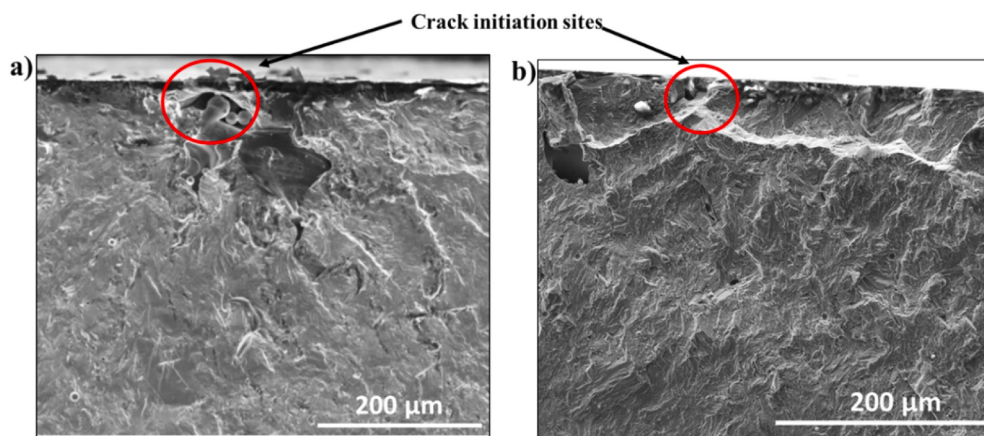


Fig. 5. (a) and (b) Fracture surface images of two specimens showing crack initiation sites.

image of the two critical pores from which the primary crack initiated. Bigger size, irregularity in shape, and proximity to each other led to stress field interactions, and resulted in crack initiation from these pores.

Fig. 6 (b), (c), and (d) provides evidence that branching of cracks occurred. Crack branching is desirable because it retards overall crack growth due to the additional energy spent during branching and

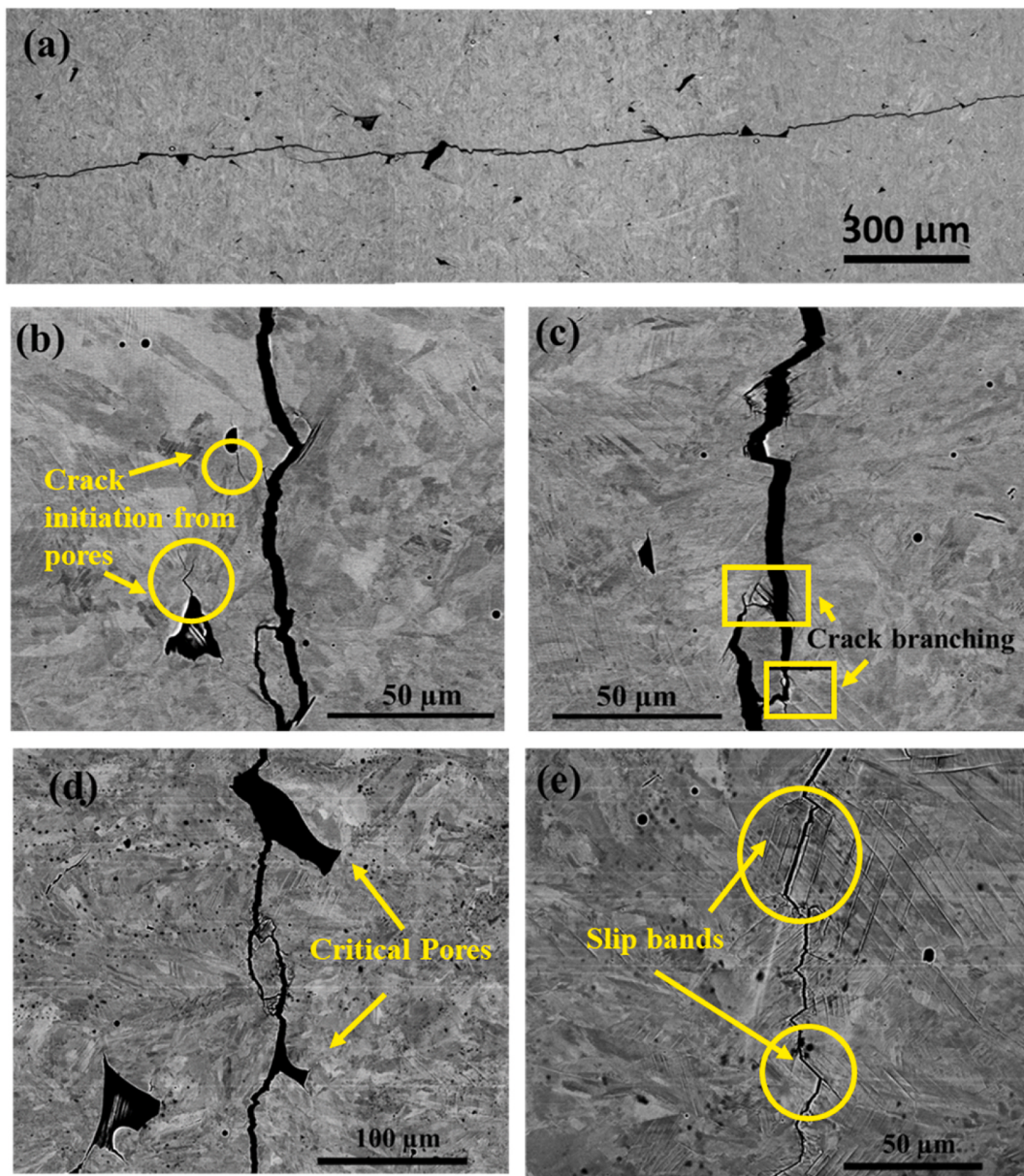


Fig. 6. (a)–(e) Back scattered images of the crack on the surface of interrupted sample.

deviation from the mode I crack path, and therefore increases overall fatigue life. Fig. 6 (e) shows the crack propagating parallel to slip bands (marked in yellow circle) in the initial stage of crack propagation. Slip bands provide an easy path for crack propagation and hence the crack follows the slip bands. However, such a propagation also increases the mode II component of loading at the crack tip, which increases the stress required for further crack advancement, thereby increasing crack propagation life.

Fig. 7 (a) – (c) present the image quality (IQ), inverse pole figure (IPF) and phase maps, respectively, of the interrupted sample near the crack. IQ and IPF maps affirm that the crack propagation path is transgranular, as the crack is moving through the grains. Deformation of ϵ dominated dual-phase CS-HEA typically shows progression of deformation mechanisms from dislocation mediated slip in γ and ϵ phases followed by transformation of γ phase to ϵ phase, and subsequent deformation of ϵ phase via activation of multiple slip systems and twinning [41,42]. As-printed CS-HEA has an initial ϵ phase fraction of 70%. However, after fatigue failure, ϵ -phase fraction increased to 95% in the crack vicinity (Fig. 7 (b)). Whereas, away from the crack tip, ϵ phase

fraction was determined as 78% (Fig. 7 (d)). Such a variation in the volume of transformed martensite reveals intense rate of transformation near the crack tip enabled by local stress concentration. The $\gamma \rightarrow \epsilon$ transformation assists local enhancement of deformation accommodation in the sample especially near the crack tip. The stress required to trigger the transformation depends on the metastability of the parent phase (γ in the present case) and, the stress concentration near the crack tip enables the proximal grains to reach transformation stress prior to distant grains which resulted in excessive transformation near the crack. Frank et al. [41] and Sinha et al. [42] have reported deformation twinning in the transformed martensitic ϵ phase. Though not extensive, marked regions in the IPF map (Fig. 7 (c)) do show twinning near the crack path in the ϵ -phase. IPF map of the grains away from the crack tip is devoid of any twins (Fig. 7 (e)). Fig. 7 (c) and (e) confirm that excessive stress proximal to the propagating crack front resulted in deformation twinning in the martensitic phase. Observed twins indicated a misorientation angle of $\sim 64^\circ$ (Fig. 7 (i) and (ii)); their similarity to twins observed in Mg [43] confirmed as contraction twins.

Mean-free path of the crack propagation typically decides the fatigue

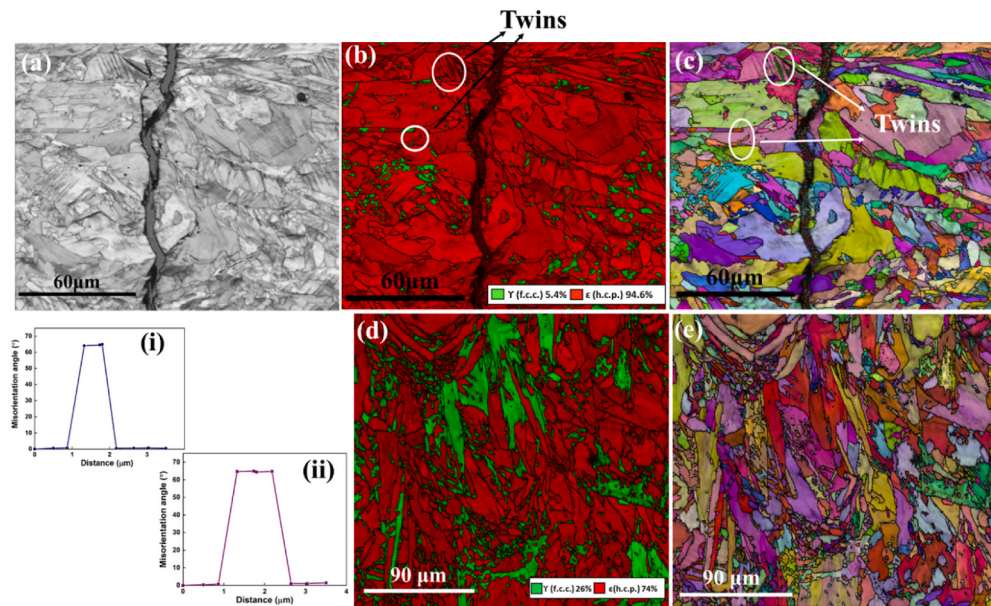


Fig. 7. (a)–(c) Image quality, phase map and inverse pole figure near the crack for the interrupted sample tested at 400 MPa and stopped after 8×10^4 cycles, (i)–(ii) misorientation angle for the twins present and (d)–(e) phase map and inverse pole figure away from the crack tip.

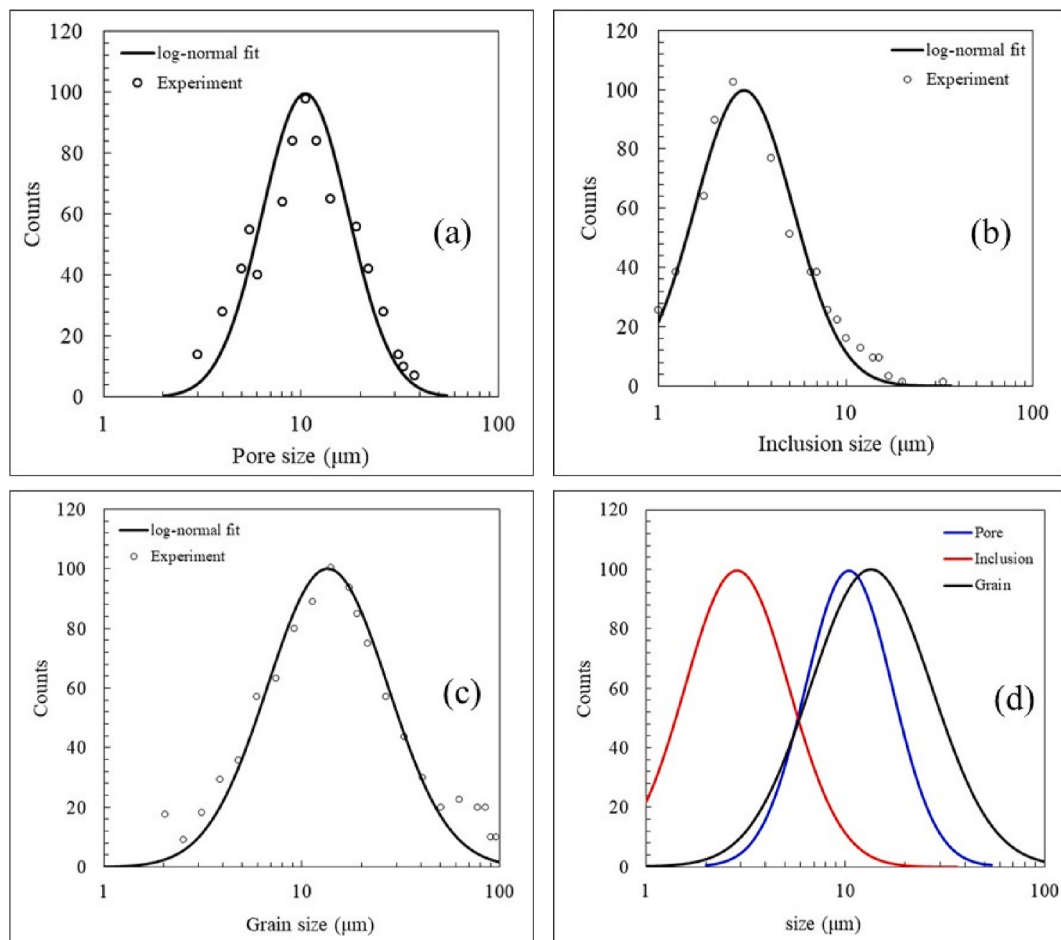


Fig. 8. Log-normal fits for the size distribution of (a) pores (b) solid-state inclusions (c) grains, and (d) comparison of the log-normal fits of all three microstructural entities.

failure life of any alloy; the crack propagation path can be engineered to alter the mean-free path. Activating different kinds of deformation mechanisms accommodates strain by enhancing local WH. In the present alloy, transformation from $\gamma \rightarrow \epsilon$ phase and subsequent twinning in ϵ phase helped to decrease the mean-free path by microcrack branching from the main crack. Hence, local WH enabled by $\gamma \rightarrow \epsilon$ transformation near the pores, a decrease in mean free path of the crack due to crack branching along the slip bands, and strain accommodation via twinning enabled excellent fatigue properties to the as-printed CS-HEA.

4.2. Fatigue life estimation model

To understand the complex interplay of crack initiation and propagation on fatigue life, the experimental results of HCF are compared with the results obtained by modeling. Most previous fatigue life estimation models applied to AM alloys considered only the distribution of pores and surface roughness [36,37,44]. Recently, Haridas et al. [17] developed a microstructure-based probabilistic fatigue life estimation model that considered the statistical size distribution of pores, solid-state inclusions and grains as well as their mutual interactions that lead to crack initiation. They emphasized the necessity of considering the embedded solid-state inclusions as potential crack initiation sites evidenced by crack initiation from an unfused powder particle near a LoF pore. Therefore, in the absence of critical pores, an unfused powder particle or a surface grain can initiate a crack. The model was applied to the current LPBF-printed CS-HEA. Sizes of pores, solid-state inclusions as well as grains were fitted to a log-normal distribution for which the probability

Table 3
Statistical parameters used for the log-normal fits of each microstructural feature.

	Pores	Solid-state inclusions	Grains
$e^{\bar{x}} (\mu\text{m})$	11.02	3.00	13.46
$e^{\sigma_{SD}} (\mu\text{m})$	1.65	1.82	2.01
Minimum (μm)	3	1	1
Maximum (μm)	38	33	96
Number density (mm^{-3})	95	80	–

Table 4

List of equations to determine fatigue crack initiation life from different microstructural features along with the probability of crack initiation.

Crack initiating features	Crack initiation cycles	Probability of crack initiation
Pore of size, D_i Grain of size, L_j	$= \frac{2M^2GW_s}{\pi} \frac{1}{(\bar{\sigma}_{a,loc} - \sigma_e)^2} \frac{1}{L}, \text{ where}$ $\bar{\sigma}_{loc} = \frac{1}{L} \int_0^L \sigma_{loc} dx$ $= \sigma_a \left[\frac{D_i k_t}{4L_j} \left\{ \left(1 + \frac{8L_j}{D_i} \right)^{1/2} - 1 \right\} + 1 \right]$ $= \frac{1}{4} \left(\frac{G' + G}{G} \right) \left(\frac{M^2 GW_I}{(\sigma_a - \sigma_e)^2} \right) \left(\frac{1}{\psi_i} \right)$ $= \frac{2M^2GW_s}{\pi} \frac{1}{(\sigma_a - \sigma_e)^2} \frac{1}{L_i}$	$\left(1 - \left(1 - \frac{SD_i}{V} \right)^{n_p(D_i)} \right) \cdot (f_g(\ln L_j) \delta \ln L)$ $\left(1 - \left(1 - \frac{S\psi_i}{V} \right)^{n_s(\psi_i)} \right) \cdot (f_g(\ln L_j) \delta \ln L)$
Inclusion of size, ψ_i Grain of size, L_j Grain of size, L_i		

Subscripts 'p', 's' and 'g' stand for pore, solid-state inclusion and grain, respectively.

M – Taylor factor.

G – Shear modulus of the material in GPa.

W_s – Specific fracture energy per unit area along the slip band in Jm^{-2} .

σ_e – Fatigue endurance limit in MPa.

σ_a – Stress amplitude of the fully reversed cyclic load in MPa.

k_t – Stress multiplication factor.

S – Surface area of the sample in m^2 .

V – Volume of the sample in m^3 .

G' – Shear modulus of the solid state inclusion in GPa.

W_I – Specific fracture energy for a unit interfacial area of the inclusion in Jm^{-2} .

$n_p(D_i)$ – number of pores in the range $\ln D_i$ to $\delta \ln D_i$.

$n_s(\psi_i)$ – number of inclusions in the range $\ln \psi_i$ to $\delta \ln \psi_i$.

density function can be represented as follows:

$$f(x) = \frac{1}{\sigma_{SD} \sqrt{2\pi}} \exp \left(-\frac{1}{2} \left(\frac{x - \bar{x}}{\sigma_{SD}} \right)^2 \right), \quad (2)$$

where x is the natural logarithm of size of either pore, solid-state inclusion or grain, σ_{SD} and \bar{x} are the standard deviation and mean of the log-normal distribution. Fig. 8 (a)–(c) show the log-normal fit obtained for the size distribution of pores, solid-state inclusions and grains, respectively. Fig. 8 (d) combined log-normal size distribution of all three microstructural features and evidenced that grains were the biggest microstructural entity, followed by pores and inclusions. Table 3 gives values of the statistical parameters for log-normal fits of each microstructural entity along with their maximum and minimum sizes as well as number density.

Following are the assumptions and attributes of the fatigue life prediction model:

1. Cracks initiate only from the sample surface irrespective of the responsible microstructural feature.
2. In the absence of critical pores and solid-state inclusions, cracks initiate from the grain itself. Solid state inclusion-grain combination and pore-grain combination are the primary entities responsible for crack initiation.
3. Mutual interaction of defects is neglected.
4. The most detrimental defect-grain combination is that associated with least fatigue life.
5. Small crack propagation theory is used to compute crack propagation life.
6. Surface roughness of the as-printed material is not considered in the model.

The fatigue life prediction model is based on the probability of each pore, solid-state inclusion and grain to exist on the sample surface as well as the probability of a specific grain to exist proximal to a defect. Table 4 summarizes the equations used to compute crack initiation life from each microstructural entity based on Tanaka and Mura [45] and Chan [46] as well as their probability of occurrence. The defect-grain combination with the least fatigue life was considered the most

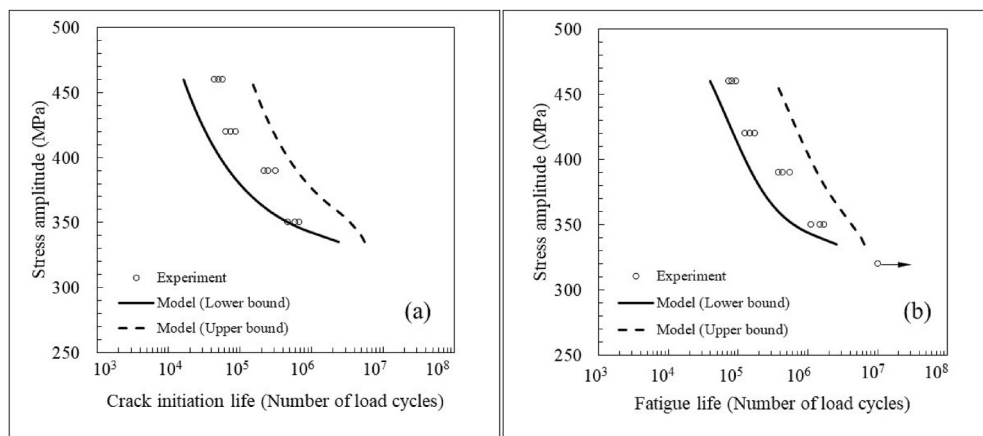


Fig. 9. (a) Comparison between experimentally obtained and model predicted values of fatigue crack initiation life vs. stress amplitude, and (b) comparison between experimentally obtained and model predicted values of fatigue life vs. stress amplitude for LPBF made CS-HEA.

Table 5
Numerical values of different parameters used in the probabilistic model.

Model parameter	Numerical value
W_s (Jm^{-2})	0.7×10^8
W_l (Jm^{-2})	3.0×10^4
Damage susceptibility factor, μ (mN^{-1})	0.55×10^{-5}
Fatigue endurance limit, σ_e (MPa)	325
Material yield strength, σ_y (MPa)	500

detrimental. Various defect-grain combinations were arranged in ascending order of fatigue life to compute cumulative probability distribution as well as fatigue life bounds for the material as a function of stress. A detailed description of the probabilistic model is included in Haridas et al. and Kapoor et al. [17,47], along with the methods to determine the cumulative probability index.

Fig. 9 (a) compares the experimentally obtained fatigue crack initiation life and the upper and lower limits of fatigue life obtained from the model. Similarly, Fig. 9 (b) compares the fatigue life of LPBF-made CS-HEA and the model values. Very good match was obtained between experiments and the probabilistic fatigue model. Table 5 gives the values of different parameters with which model data were optimized with experimental data. The lower bound of the model corresponds to the minimum value of cumulative probability index, whereas the upper bound signifies a cumulative probability index of 1. The values of W_s and W_l vary with material and were reported to fall in the range 10^4 – 10^6 Jm^{-2} [48]. The higher value of W_s obtained for the current CS-HEA (0.7×10^8 Jm^{-2}) indicated the need for extra energy for crack initiation from the proximal grain of a pore by dislocation activity. In our previous study on an AM Al alloy [17], the value of W_s was obtained as 1×10^6 Jm^{-2} which is almost two orders of magnitude lower than the value obtained for the present TRIP CS-HEA. Such higher value of W_s obtained for CS-HEA is an indirect indication that sustained hardening developed ahead of micro-voids due to persistent TRIP. Similarly, the value of damage susceptibility factor, μ , fits in the range of 10^{-3} to 10^{-6} m^2J^{-1} for most of the metals [47,49]. The best fit between experimental and model predictions was obtained for a value of μ at 5.5×10^{-4} Jm^{-2} . A much lower value of μ indicates that crack progression inside the material is sluggish and results in higher crack propagation life. Such a sustained crack propagation behavior is attributed to crack branching and sustained metastability-driven hardening due to γ (f.c.c.) \rightarrow ϵ (h.c.p.) transformation and justifies the observations presented previously in discussion regarding crack initiation and propagation during HCF [10]. Favorable values of both parameters (higher W_s and lower μ) in the present material with embedded pores and inclusions indicates a material with excellent damage tolerant property.

Fig. 10 (a) illustrates the cumulative probability distribution of LPBF fabricated CS-HEA obtained from the probabilistic model at stress levels of 350 MPa, 400 MPa and 450 MPa. The cumulative probability value signifies the possibility of the material to fail below a specific number of load cycles at a certain load. In other words, the LPBF fabricated CS-HEA sample will never fail below 6.3×10^5 load cycles, and the sample will never sustain above 3.3×10^6 load cycles at 350 MPa. Leftward shifting of the cumulative probability curve with an increase in stress amplitude level indicates a lower fatigue life for the material at higher stresses (Fig. 10 (a)). Yi et al. [50] quantitatively analyzed the scatter in fatigue life from the cumulative probability distribution using a three-parameter Weibull distribution function as follows,

$$F = 1 - \exp\left(-\left(\frac{N - N_0}{N_c - N_0}\right)^b\right), \quad (3)$$

where F is the cumulative probability distribution function, b is the Weibull modulus, and N_0 and N_c are the fatigue threshold and characteristic fatigue life of the material for a specific stress amplitude. Rearranging the above equation and applying natural logarithm, Eqn. (3) modifies to

$$\ln(-\ln(1 - F)) = b \ln(N - N_0) - b \ln(N_c - N_0). \quad (4)$$

Weibull modulus b signifies the scatter in fatigue life, whereas N_0 signifies the number of load cycles below which material is safe under cyclic load. Three-parameter Weibull distribution function at a specific load is determined by obtaining the best possible straight line fit for Eqn. (4). Fig. 10 (b) shows the three-parameter Weibull distribution function fits corresponding to the stress levels indicated in Fig. 10 (a). The higher value of Weibull modulus, b , at 350 MPa when compared to 450 MPa specifies that the scatter in fatigue life is minimal at 350 MPa. To obtain a complete picture of three parameters associated with Weibull distribution function, their variation with stress is plotted in Fig. 10 (c). An increase in Weibull modulus with a decrease in stress signifies that fatigue life scatter increases with increase in stress and vice versa. Additionally, reducing trend of N_0 and N_c verifies fatigue life increment with decrease in the magnitude of stress amplitude.

5. Conclusions

Alloy design strategies that facilitate the activation of multiple deformation mechanisms are required in AM, which produces components with process induced defects such as pores and inclusions. Metastable alloys have lower SFE and thus are predisposed to strain accommodation via deformation mechanisms such as TRIP and TWIP. Fatigue response of a metastable high entropy alloy made by LPBF was

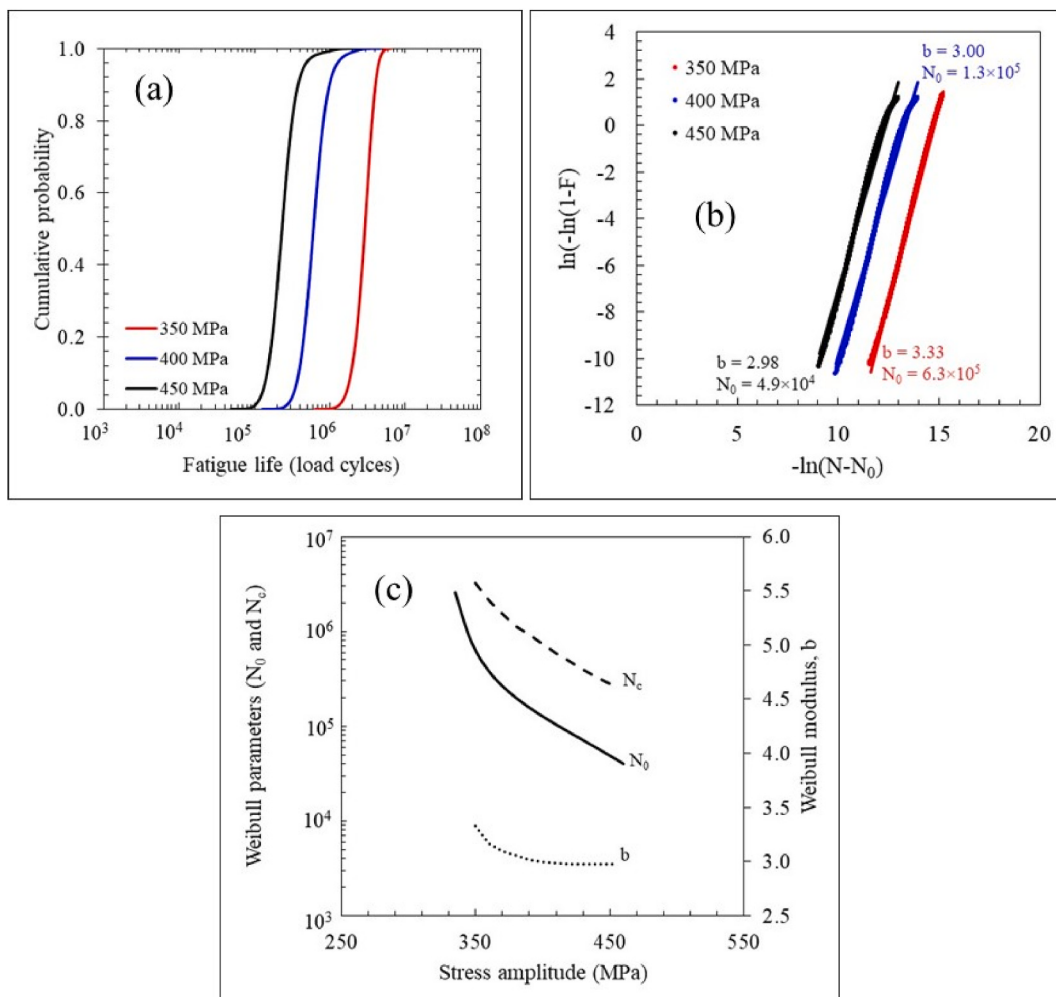


Fig. 10. (a) Plot of cumulative probability distribution for CS-HEA at stress amplitudes of 350, 400 and 450 MPa, (b) Weibull distribution function fits corresponding to the cumulative distribution functions shown in (a), and (c) fatigue threshold and fatigue characteristic life with stress amplitudes for CS-HEA.

investigated. The material showed excellent fatigue behavior with an endurance limit corresponding to $\sigma_a/\sigma_y = 0.65$. The results indicated that local WH enabled by $\gamma \rightarrow \epsilon$ transformation triggered by local stress concentration near the pores, a decrease in mean free path of the crack due to crack branching along the slip bands and strain accommodation via twinning resulted in excellent fatigue properties of the as-printed CS-HEA despite the pores. Furthermore, a probabilistic model based on the statistical size distribution of pores, solid-state inclusions, grains and their mutual interactions was used to estimate the fatigue life of the material. The damage and energy indicators of the model suggest a delayed crack initiation and prolonged crack propagation life for the material, thereby supports and justifies the experimental observations.

Data availability statement

The raw/processed data required to reproduce these findings cannot be shared at this time as the data also forms part of an ongoing study.

CRediT authorship contribution statement

Priyanshi Agrawal: Conceptualization, Data curation, Formal analysis, Methodology, Writing – original draft. **Ravi Sankar Haridas:** Conceptualization, Data curation, Formal analysis, Methodology, Writing – original draft. **Saket Thapliyal:** Methodology, Writing – review & editing. **Surekha Yadav:** Methodology, Writing – review & editing. **Rajiv S. Mishra:** Conceptualization, Project administration,

Resources, Supervision, Writing – review & editing. **Brandon A. McWilliams:** Project administration, Writing – review & editing. **Kyu C. Cho:** Project administration, Writing – review & editing.

Declaration of competing interest

The authors declare that they have no known competing financial interests or personal relationships that could have appeared to influence the work reported in this paper.

Acknowledgements

This current study was performed under cooperation agreement between the Army Research Laboratory and University of North Texas (W911NF1920011). The authors thank Materials Research Facility for allowing access to microscopy facilities at the University of North Texas.

References

- [1] I. Paoletti, Mass customization with additive manufacturing: new perspectives for multi performative building components in architecture, Procedia Eng. 180 (2017) 1150–1159, <https://doi.org/10.1016/j.proeng.2017.04.275>.
- [2] U.M. Dilberoglu, B. Gharehpapagh, U. Yaman, M. Dolen, The role of additive manufacturing in the era of industry 4.0, Procedia Manuf. 11 (2017) 545–554, <https://doi.org/10.1016/j.promfg.2017.07.148>.
- [3] G.H. Loh, E. Pei, D. Harrison, M.D. Monzón, An overview of functionally graded additive manufacturing, Addit. Manuf. 23 (2018) 34–44, <https://doi.org/10.1016/j.addma.2018.06.023>.

- [4] S. Thapliyal, M. Komarasamy, S. Shukla, L. Zhou, H. Hyer, S. Park, Y. Sohn, R.S. Mishra, An Integrated Computational Materials Engineering-Anchored Closed-Loop Method for Design of Aluminum Alloys for Additive Manufacturing, *Materialia*, 2019, p. 100574, <https://doi.org/10.1016/j.mtla.2019.100574>.
- [5] T. DebRoy, H.L. Wei, J.S. Zuback, T. Mukherjee, J.W. Elmer, J.O. Milewski, A.M. Beese, A. Wilson-Heid, A. De, W. Zhang, Additive manufacturing of metallic components – process, structure and properties, *Prog. Mater. Sci.* 92 (2018) 112–224, <https://doi.org/10.1016/j.pmatsci.2017.10.001>.
- [6] H. Shipley, D. McDonnell, M. Culleton, R. Coull, R. Lupoi, G.O. Donnell, D. Trimble, International Journal of Machine Tools and Manufacture Optimisation of process parameters to address fundamental challenges during selective laser melting of Ti-6Al-4V: a review, *Int. J. Mach. Tool Manufact.* 128 (2018) 1–20, <https://doi.org/10.1016/j.ijmachtools.2018.01.003>.
- [7] P. Agrawal, S. Shukla, S. Thapliyal, P. Agrawal, S.S. Nene, R.S. Mishra, B.A. McWilliams, K.C. Cho, Microstructure–property correlation in a laser powder bed fusion processed high-strength AF-9628 steel, *Adv. Eng. Mater.* (2020) 1–8, <https://doi.org/10.1002/adem.202000845>.
- [8] S.S. Nene, M. Frank, K. Liu, S. Sinha, R.S. Mishra, B. McWilliams, K.C. Cho, Reversed strength-ductility relationship in microstructurally flexible high entropy alloy, *Scripta Mater.* 154 (2018) 163–167, <https://doi.org/10.1016/j.scriptamat.2018.05.043>.
- [9] S.S. Nene, M. Frank, K. Liu, R.S. Mishra, B.A. McWilliams, K.C. Cho, Extremely high strength and work hardening ability in a metastable high entropy alloy, *Sci. Rep.* 8 (2018) 1–8, <https://doi.org/10.1038/s41598-018-28383-0>.
- [10] K. Liu, S.S. Nene, M. Frank, S. Sinha, R.S. Mishra, Extremely high fatigue resistance in an ultrafine grained high entropy alloy, *Appl. Mater. Today* 15 (2019) 525–530, <https://doi.org/10.1016/j.apmt.2019.04.001>.
- [11] S. Thapliyal, S.S. Nene, P. Agrawal, T. Wang, C. Morphew, R.S. Mishra, B.A. McWilliams, K.C. Cho, Damage-tolerant, corrosion-resistant high entropy alloy with high strength and ductility by laser powder bed fusion additive manufacturing, *Addit. Manuf.* 36 (2020) 101455, <https://doi.org/10.1016/J.ADDMA.2020.101455>.
- [12] Z. Li, K.G. Pradeep, Y. Deng, D. Raabe, C.C. Tasan, Metastable high-entropy dual-phase alloys overcome the strength-ductility trade-off, *Nature* 534 (2016) 227–230, <https://doi.org/10.1038/nature17981>.
- [13] P. Agrawal, S. Thapliyal, S.S. Nene, R.S. Mishra, B.A. McWilliams, K.C. Cho, Excellent strength-ductility synergy in metastable high entropy alloy by laser powder bed additive manufacturing, *Addit. Manuf.* 32 (2020).
- [14] L. Carneiro, B. Jalalahmadi, A. Ashtekar, Y. Jiang, Cyclic deformation and fatigue behavior of additively manufactured 17 – 4 PH stainless steel, *Int. J. Fatig.* 123 (2019) 22–30, <https://doi.org/10.1016/j.ijfatigue.2019.02.006>.
- [15] K.S. Chan, A. Peralta-Duran, A methodology for predicting surface crack nucleation in additively manufactured metallic components, *Metall. Mater. Trans. A Phys. Metall. Mater. Sci.* 50 (2019) 4378–4387, <https://doi.org/10.1007/s11661-019-05309-7>.
- [16] P. Kumar, O. Prakash, U. Ramamurty, Micro-and meso-structures and their influence on mechanical properties of selectively laser melted Ti-6Al-4V, *Acta Mater.* 154 (2018) 246–260, <https://doi.org/10.1016/j.actamat.2018.05.044>.
- [17] R.S. Haridas, S. Thapliyal, P. Agrawal, R.S. Mishra, Defect-based probabilistic fatigue life estimation model for an additively manufactured aluminum alloy, *Mater. Sci. Eng.* 798 (2020) 140082, <https://doi.org/10.1016/j.msea.2020.140082>.
- [18] J. Suryawanshi, K.G. Prashanth, U. Ramamurty, Mechanical behavior of selective laser melted 316L stainless steel, *Mater. Sci. Eng.* 696 (2017) 113–121, <https://doi.org/10.1016/j.msea.2017.04.058>.
- [19] C. Pei, D. Shi, H. Yuan, H. Li, Materials Science & Engineering A Assessment of mechanical properties and fatigue performance of a selective laser melted nickel-base superalloy Inconel 718, *Mater. Sci. Eng.* 759 (2019) 278–287, <https://doi.org/10.1016/j.msea.2019.05.007>.
- [20] M. Frank, Y. Chen, S.S. Nene, S. Sinha, K. Liu, K. An, R.S. Mishra, Investigating the deformation mechanisms of a highly metastable high entropy alloy using in-situ neutron diffraction, *Mater. Today Commun.* (2019), <https://doi.org/10.1016/j.mtcomm.2019.100858>.
- [21] K. Liu, S.S. Nene, M. Frank, S. Sinha, R.S. Mishra, Metastability-assisted fatigue behavior in a friction stir processed dual-phase high entropy alloy, *Mater. Res. Lett.* 6 (2018) 613–619, <https://doi.org/10.1080/21663831.2018.1523240>.
- [22] A. Glage, A. Weidner, H. Biermann, Effect of austenite stability on the low cycle fatigue behavior and microstructure of high alloyed metastable austenitic cast TRIP-steels, *Procedia Eng.* 2 (2010) 2085–2094, <https://doi.org/10.1016/j.proeng.2010.03.224>.
- [23] R.S. Mishra, S.S. Nene, M. Frank, S. Sinha, K. Liu, S. Shukla, Metastability driven hierarchical microstructural engineering: overview of mechanical properties of metastable complex concentrated alloys, *J. Alloys Compd.* 842 (2020) 155625, <https://doi.org/10.1016/j.jallcom.2020.155625>.
- [24] M.T. Todinov, A probabilistic method for predicting fatigue life controlled by defects, *Mater. Sci. Eng.* 255 (1998) 117–123, [https://doi.org/10.1016/s0921-5093\(98\)00772-2](https://doi.org/10.1016/s0921-5093(98)00772-2).
- [25] K.S. Chan, Scaling laws for fatigue crack, *Metall. Trans. A* 24 (1993) 2473–2486, <https://doi.org/10.1007/BF02646526>.
- [26] A. de Bussac, J.C. Lautridou, A probabilistic model for prediction OF lcf surface crack initiation IN pm alloys, *Fatig. Fract. Eng. Mater. Struct.* 16 (1993) 861–874, <https://doi.org/10.1111/j.1460-2695.1993.tb00125.x>.
- [27] J.Z. Yi, Y.X. Gao, P.D. Lee, T.C. Lindley, Microstructure-based fatigue life prediction for cast A356-T6 aluminum-silicon alloys, *Metall. Mater. Trans. B Process Metall. Mater. Process. Sci.* 37 (2006) 301–311, <https://doi.org/10.1007/BF02693159>.
- [28] D.L. McDowell, K. Gall, M.F. Horstemeyer, J. Fan, Microstructure-based fatigue modeling of cast A356-T6 alloy, *Eng. Fract. Mech.* 70 (2003) 49–80, [https://doi.org/10.1016/S0013-7944\(02\)00021-8](https://doi.org/10.1016/S0013-7944(02)00021-8).
- [29] P.S. De, C.M. Obermark, R.S. Mishra, Development of a reversible bending fatigue test bed to evaluate bulk properties using sub-size specimens, *J. Test. Eval.* 36 (2008) 101669, <https://doi.org/10.1520/jte101669>.
- [30] C. Teng, D. Pal, H. Gong, K. Zeng, K. Briggs, N. Patil, B. Stucker, A review of defect modeling in laser material processing, *Addit. Manuf.* 14 (2017) 137–147, <https://doi.org/10.1016/j.addma.2016.10.009>.
- [31] S.A. David, J.M. Vitek, Correlation between solidification parameters and weld microstructures, *Int. Mater. Rev.* 34 (1989) 213–245, <https://doi.org/10.1179/imr.1989.34.1.213>.
- [32] M.J. Birmingham, D.H. StJohn, J. Krynen, S. Tedman-Jones, M.S. Dargusch, Promoting the columnar to equiaxed transition and grain refinement of titanium alloys during additive manufacturing, *Acta Mater.* 168 (2019) 261–274, <https://doi.org/10.1016/j.actamat.2019.02.020>.
- [33] C.A. Siqueira, N. Cheung, A. Garcia, Solidification thermal parameters affecting the columnar-to-equiaxed transition, *Metall. Mater. Trans. A Phys. Metall. Mater. Sci.* 33 (2002) 2107–2118, <https://doi.org/10.1007/s11661-002-0042-4>.
- [34] S. Lee, J. Pegues, N. Shamsaei, Fatigue behavior and modeling for additive manufactured 304L stainless steel: the effect of surface roughness, *Int. J. Fatig.* (2020) submitted for publication.
- [35] M. Zhang, C.N. Sun, X. Zhang, J. Wei, D. Hardacre, H. Li, Predictive models for fatigue property of laser powder bed fusion stainless steel 316L, *Mater. Des.* 145 (2018) 42–54, <https://doi.org/10.1016/j.matdes.2018.02.054>.
- [36] R. Biswal, A.K. Syed, X. Zhang, Assessment of the effect of isolated porosity defects on the fatigue performance of additive manufactured titanium alloy, *Addit. Manuf.* 23 (2018) 433–442, <https://doi.org/10.1016/j.addma.2018.08.024>.
- [37] A. Yadollahi, M.J. Mahtabi, A. Khalili, H.R. Doude, J.C. Newman, Fatigue life prediction of additively manufactured material: effects of surface roughness, defect size, and shape, *Fatig. Fract. Eng. Mater. Struct.* 41 (2018) 1602–1614, <https://doi.org/10.1111/ffe.12799>.
- [38] M. Tang, P.C. Pistorius, Fatigue life prediction for AlSi10Mg components produced by selective laser melting, *Int. J. Fatig.* 125 (2019) 479–490, <https://doi.org/10.1016/j.ijfatigue.2019.04.015>.
- [39] S. Suresh, Fatigue of Materials, 2002, <https://doi.org/10.1201/9780203910399.ch14>.
- [40] S.S. Nene, M. Frank, K. Liu, S. Sinha, R.S. Mishra, B. McWilliams, K.C. Cho, Reversed strength-ductility relationship in microstructurally flexible high entropy alloy, *Scripta Mater.* 154 (2018) 163–167, <https://doi.org/10.1016/j.scriptamat.2018.05.043>.
- [41] M. Frank, Y. Chen, S.S. Nene, S. Sinha, K. Liu, K. An, R.S. Mishra, Investigating the deformation mechanisms of a highly metastable high entropy alloy using in-situ neutron diffraction, *Mater. Today Commun.* 23 (2020) 100858, <https://doi.org/10.1016/j.mtcomm.2019.100858>.
- [42] S. Sinha, S.S. Nene, M. Frank, K. Liu, R.A. Lebensohn, R.S. Mishra, Deformation mechanisms and ductile fracture characteristics of a friction stir processed transformative high entropy alloy, *Acta Mater.* 184 (2020) 164–178, <https://doi.org/10.1016/j.actamat.2019.11.056>.
- [43] K.Y. Xie, Z. Alam, A. Caffee, K.J. Hemker, Deformation behavior of Mg single crystals compressed along c-axis, *Magnes. Technol.* 2016, John Wiley & Sons, Ltd, 2016, pp. 209–211, <https://doi.org/10.1002/978119274803.ch42>.
- [44] R. Biswal, X. Zhang, A.K. Syed, M. Awd, J. Ding, F. Walther, S. Williams, Criticality of porosity defects on the fatigue performance of wire + arc additive manufactured titanium alloy, *Int. J. Fatig.* 122 (2019) 208–217, <https://doi.org/10.1016/j.ijfatigue.2019.01.017>.
- [45] K. Tanaka, T. Mura, A theory of fatigue crack initiation at inclusions, *Mettal. Trans. A* 13 (1982) 117–123, <https://doi.org/10.1007/BF02642422>.
- [46] K.S. Chan, A microstructure-based fatigue-crack-initiation model, *Mettal. Mater. Trans. A, Phys. Metall. Mater. Sci.* 34 (2003) 16–43.
- [47] R. Kapoor, V.S.H. Rao, R.S. Mishra, J.A. Baumann, G. Grant, Probabilistic fatigue life prediction model for alloys with defects: applied to A206, *Acta Mater.* 59 (2011) 3447–3462, <https://doi.org/10.1016/j.actamat.2011.02.019>.
- [48] K.S. Chan, A microstructure-based fatigue-crack-initiation model, *Mettal. Mater. Trans. 34A* (2003) 43–58.
- [49] A. Shyam, J.E. Allison, C.J. Szczepanski, T.M. Pollock, J.W. Jones, Small fatigue crack growth in metallic materials : a model and its application to engineering alloys, 55, <https://doi.org/10.1016/j.actamat.2007.08.022>, 2007, 6606–6616.
- [50] J.Z. Yi, P.D. Lee, T.C. Lindley, T. Fukui, Statistical Modeling of Microstructure and Defect Population Effects on the Fatigue Performance of Cast A356-T6 Automotive Components, vol. 432, 2006, pp. 59–68, <https://doi.org/10.1016/j.msea.2006.07.003>.